PERFORMANCE OF HYBRID VEHICLES EQUIPPED WITH TOROIDAL CVT

Breno Raizer, breno_raizer@hotmail.com
Franco Giuseppe Dedini, dedini@fem.unicamp.br
Marcelo G. Tanikawa, marcelo.tanikawa@gmail.com
Bruno Rodrigues de Sunti, brunodesunti@hotmail.com
Reynaldo Barros de Souza, reybs@fem.unicamp.br
DPM - FEM - UNICAMP

Abstract. *The growth of environmental concerns has resulted in a search for significantly cleaner and more efficient vehicles. This search highly depended on the development of advanced technologies, like electric and hybrid electric vehicles (HEV's). Often, the combination of two or more sources of mechanical power requires a sophisticated power transmission system, capable of adjust the levels of rotation and torque between the sources of power, and between them and the trajectory requirements of the vehicle. In order to achieve its purpose, CVTs have recently been used on hybrid vehicles. In this work, the main goal is to evaluate the impact that a Toroidal-CVT (T-CVT) has in the performance of a hybrid vehicle's powertrain. A full mathematical modeling of the power transmission through the elasto-hydrodinamic lubricated contacts is applied to evaluate the T-CVT efficiency during the HEV acceleration. The results points that the good positioning of the electrical engine on the power train have a directly influence in its contribution for the vehicle performance.*

Keywords*: Toroidal CVT, Hybrid Vehicles, HEV, Simulation*

1. INTRODUCTION

Even today the automotive market is highly dependent on internal combustion engines (ICE). The progress of electric vehicles (EV) in this market is limited by the advance in energy storage technology, in other words, the development of batteries capable of storing large amounts of energy and of quickly respond to changes in power demand. Meanwhile, the increasing requirement to reduce emissions and search for cleaner and renewable sources of energy has pushed the market to seek alternative solutions.

Electric vehicles have several advantages over conventional ICE vehicles, such as high-energy efficiency and zero environmental pollution during operation (Bartilotti *et al.*, 2009). However the autonomy, measured by the operational limit per battery charge, is much lower than the autonomy of an ICE vehicle. That is because battery has a lower energy density compared to gasoline, alcohol, diesel and other chemical fuels. Hybrid electric vehicle (HEV) has a better balance between conventional and electrical systems advantages (Ehsani *et al.*, 2005). Is important to say that hybrid vehicles projects already became available a long time ago, and the reason for its increasing use nowadays is the aggressive marketing, focused on fuel consumption and environmental impacts reduction (Bartilotti *et al.*, 2009).

Another attempt in order to minimize consumption and the environmental impact of ICEs was through is optimization using drive trains systems equipped with continuously variable transmissions (CVTs), which are being investigated for this purpose (Carbone *et al.*, 2004). Though CVTs seems to be relative costly in comparison to automatic transmissions (Tenberge & Möckel, 2002), is important to consider that the benefits of using CVTs include fuel savings, reduced exhaust emissions, smooth power delivery, noise reduction and comfort (Nikas, 2002).

In traction drive CVTs, torque is transmitted through Elasto-Hydrodynamic (EHD) fluid films between the contact surfaces (Forti, 2003). The contact point positions are a function of the system geometry, and determine the system transmission Ratio (TR). And among the many layouts of CVTs, dual-cavity Half Toroidal CVT (HT-CVT) is found to be appropriate for automotive powertrain applications due high efficiency and torque transmission capability (Zhang *et al.*, 2000). Moreover the particular geometry of the toroidal traction drive makes it able to rapidly adjust its speed ratio to the request of the driver, thus improving the driving comfort (Carbone *et al.*, 2004). The elasto-hydrodinamic lubricated contacts occur on the power roller surface, pressed between the input disk and the output disk. The continuously change in the TR is achieved by tilting the angle of the power roller axis with respect to the disk axis.

Nowadays both technical solutions are being developed in other to achieve a better usage of our natural resources. And knowing so, this work is the initial steps of the creation of a mathematical model capable of predicting the behavior of a automotive system that aggregates both technologies.

2. MATHEMATICAL MODEL OF T-CVT

The mathematical model used to simulate a T-CVT behavior is divided in three parts: modeling of system geometry, torque transmission and peripheral systems. The geometric model must provide for possible misalignment in the rollers

axes in order to contemplate the effects of Side-slip, as well of Slip and Spin. The torque transmission model must predict the Elasto-Hydrodynamic (EHD) behavior of the lubrication fluid in the contact area, relating components surface velocities and pressure profile in contact area with the tangential forces transmitted. The modeled peripheral systems include the Loading Cam, responsible for the system pressurization, and a model to predict the bearing losses.

Figure 1 illustrates the basic geometry of a toroidal transmission. A T-CVT is composed of three main components: input disk, power roller and output disk. The space formed between the input and output discs is called toroidal cavity. For higher torque capacity, two or more rollers per cavity may be used, as well additional cavities (Zhang *et al.*, 2000). As shown in the Fig.1, the dimension and geometry of the T-CVT are defined by the Cavity Radius (R), Torus Radius (Y_0), Half-cone Angle (γ), Roller Profile Radius (r_a). For mathematical modeling purposes, the Half-cone Angle (γ) can be replaced by Roller Plane Height (h), facilitating the equationing of geometrical misalignments (Raizer and Dedini, 2009; Raizer, 2010).

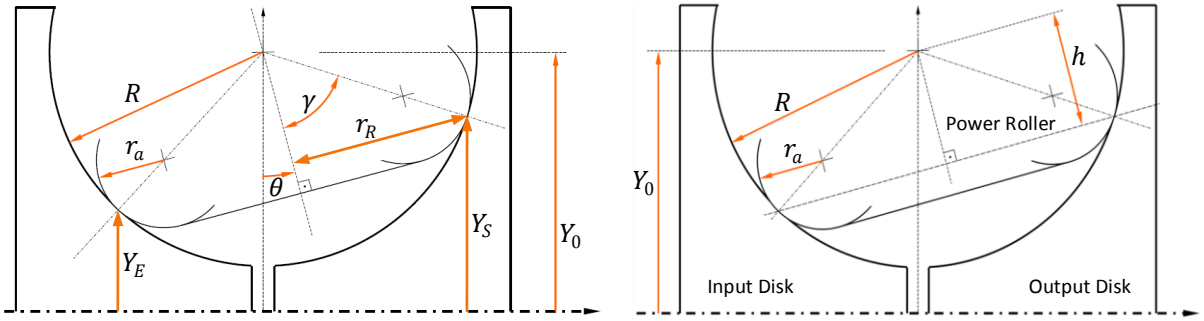

Figure 1. Basic geometric modeling of T-CVT cavity.

2.1. Geometric Modeling of T-CVT

The theoretical gear ratio, also called Ideal Transmission Ratio (Ideal TR, RT_{Tid}), depends on the input contact point height (Y_E) and output contact point height (Y_S), as shown in Eq. 1. Equations 2, 3 and 4 (Raizer and Dedini, 2009) are used to evaluate the contact points positions for any configuration of tilt angle (θ) or misalign angles (α and β).

$$RT_{Tid} = \frac{Y_E}{Y_S} \tag{1}$$

$$Y_E = Y_0 - \frac{h \cdot cos\,\beta \cdot cos\,\theta + (cos\,\alpha \cdot sin\,\theta \cdot cos\,\beta - sin\,\alpha \cdot sin\,\beta) \cdot \sqrt{R^2 \cdot G - h^2}}{G} \tag{2}$$

$$Y_S = Y_0 - \frac{h \cdot cos\,\beta \cdot cos\,\theta - (cos\,\alpha \cdot sin\,\theta \cdot cos\,\beta - sin\,\alpha \cdot sin\,\beta) \cdot \sqrt{R^2 \cdot G - h^2}}{G} \tag{3}$$

$$G = 1 - cos^2\,\alpha \cdot sin^2\,\beta - sin^2\,\alpha \cdot cos^2\,\beta \cdot sin^2\,\theta - 0{,}5 \cdot sin\,2\alpha \cdot sin\,2\beta \cdot sin\,\theta \tag{4}$$

Besides providing a Side-slip condition, α and β changes the effective geometry of the contact. The hypothesis adopted was that the angular gap between the planes doesn't change the elliptical geometry of the contact, and thus the effective radius of the roller surface in the direction of one of the main planes of the disk can be estimated by a weighted average of the principal radii of surfaces, function of the misalignment between the roller and the disk rolling direction (Φ). And so, the principal radii of curvature from the surfaces, written in the disc contact reference, can be written as shown in Eq.5 and Eq.6. Equation 7 and Eq. 8 contains the procedure to calculate the Φ value for the input contat (Φ_E) and for the output contact (Φ_S), using the information from the coordinate transformation matrices arranged in Eq.9, Eq.10, Eq.11 and Eq.12 (Raizer, 2010).

$$\begin{bmatrix} R_{Dx} \\ R_{Dy} \end{bmatrix}_i = R \cdot \begin{bmatrix} Y_i/(Y_0 - Y_i) \\ -1 \end{bmatrix} \tag{5}$$

$$\begin{bmatrix} R_{Rox} \\ R_{Roy} \end{bmatrix}_i = \begin{bmatrix} cos^2\,\Phi_i & sin^2\,\Phi_i \\ sin^2\,\Phi_i & cos^2\,\Phi_i \end{bmatrix} \cdot \begin{bmatrix} r_R \\ r_a \end{bmatrix} = \begin{bmatrix} cos^2\,\Phi_i & sin^2\,\Phi_i \\ sin^2\,\Phi_i & cos^2\,\Phi_i \end{bmatrix} \cdot \begin{bmatrix} \sqrt{R^2 - h^2} \\ r_a \end{bmatrix} \tag{6}$$

$$\begin{bmatrix} cos\,\Phi_E & -sin\,\Phi_E & 0 \\ sin\,\Phi_E & cos\,\Phi_E & 0 \\ 0 & 0 & 1 \end{bmatrix} = [S_{CD}]_E \cdot [S_{D0}]_E \cdot ([S_{CR}]_E \cdot [S_{R0}])^{-1} \tag{7}$$

$$\begin{bmatrix} cos\,\Phi_S & sin\,\Phi_S & 0 \\ -sin\,\Phi_S & cos\,\Phi_S & 0 \\ 0 & 0 & 1 \end{bmatrix} = [S_{CD}]_S \cdot [S_{D0}]_S \cdot ([S_{CR}]_S \cdot [S_{R0}])^{-1} \tag{8}$$

$$[S_{D0}]_E = \begin{bmatrix} 1 & 0 & 0 \\ 0 & 1 & 0 \\ 0 & 0 & 1 \end{bmatrix};\ [S_{D0}]_S = \begin{bmatrix} -1 & 0 & 0 \\ 0 & 1 & 0 \\ 0 & 0 & -1 \end{bmatrix} \tag{9}$$

$$[S_{R0}]^{-1} = \begin{bmatrix} cos\,\alpha & 0 & sin\,\alpha \\ 0 & 1 & 0 \\ -sin\,\alpha & 0 & cos\,\alpha \end{bmatrix} \cdot \begin{bmatrix} cos\,\theta & -sin\,\theta & 0 \\ sin\,\theta & cos\,\theta & 0 \\ 0 & 0 & 1 \end{bmatrix} \cdot \begin{bmatrix} 1 & 0 & 0 \\ 0 & cos\,\beta & -sin\,\beta \\ 0 & sin\,\beta & cos\,\beta \end{bmatrix} \tag{10}$$

$$[S_{CR}]_i = \begin{bmatrix} -sin\,\varphi_i & 0 & -cos\,\varphi_i \\ -(h/R)\,cos\,\varphi_i & \sqrt{R^2-h^2}/R & (h/R)\,sin\,\varphi_i \\ -(r_R/R)\,cos\,\varphi_i & h/R & \left(\sqrt{R^2-h^2}/R\right) sin\,\varphi_i \end{bmatrix} \tag{11}$$

$$[S_{CD}]_i = \frac{1}{R}\begin{bmatrix} 0 & 0 & R \\ (Y_0 - Y_i) & |X_i| & 0 \\ -|X_i| & (Y_0 - Y_i) & 0 \end{bmatrix} \tag{12}$$

The angle φ_i (φ_E for the input contact and φ_S for the output contact) is the angular position of the point of contact written in the Roller coordinate system, and is given by Eq.13 as a function of the transformation matrix from the global coordinate system to the roller coordinate system (S_{R0}), the geometric parameters (R, Y_0 and h) and the contact point position (X_i and Y_i).

$$\begin{bmatrix} cos\,\varphi_i \\ 0 \\ -sin\,\varphi_i \end{bmatrix} = \frac{1}{\sqrt{R^2-h^2}} \cdot \left([S_{R0}] \cdot \begin{bmatrix} X_i \\ Y_i - Y_0 \\ 0 \end{bmatrix} + \begin{bmatrix} 0 \\ h \\ 0 \end{bmatrix} \right) \tag{13}$$

2.3. Modeling of lubrication and contact forces

Considering a "quasi-identical" problem, or in other words, a situation where the bodies in contact have nearly the same elastic properties, the contact problem can be solved independently for the tangential efforts and for the normal efforts (Forti, 2003), thus facilitating their resolution. Despite the flow of lubricant slightly change the pressure profile in the contact area (Nonato, 2009), it is common to use the hertzian contact resolution directly as a first approach (Attia, 2005; Carbone *et al.*, 2004; Forti, 2003; Nikas, 2002; Zhang *et al.*, 2000). The results of the hertzian contact theory may also be used together with the rolling bearings life prediction models in order to estimate the T-CVT life time with little error (Lee *et al.*, 2004; Nikas, 2002;Coy *et al.*, 1976). The resolution of the hertzian contact problem can be easily found in nowadays bibliographic (Harris and Kotzalas, 2006; Attia, 2005; Carbone *et al.*, 2004; Forti, 2003; Nikas, 2002; Zhang *et al.*, 2000). Figure 2 has information concerning the geometrical modeling of the surfaces near the contact point and the resultant elliptical contact area.

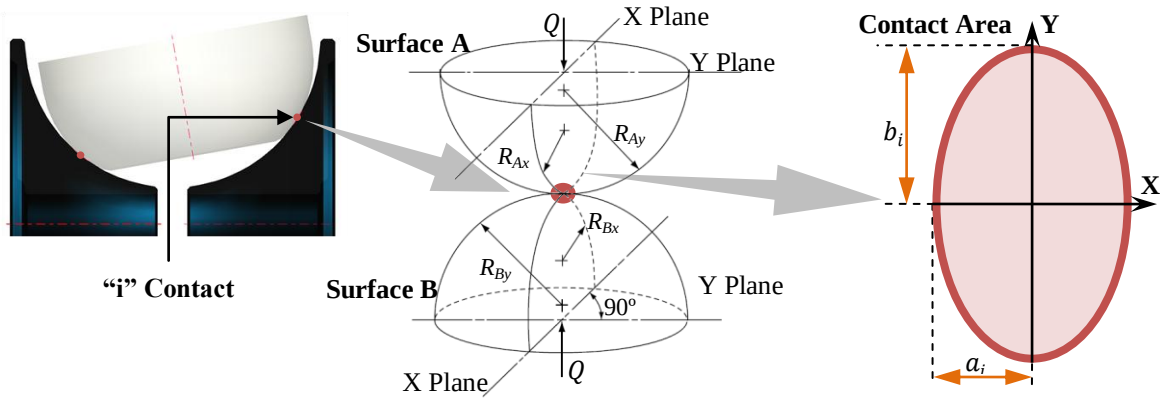

Figure 2. Contact area and local surface geometry.

Assuming a negligible relative velocity due material deformation (on both tangential and normal directions) of the elastic bodies and a nearly constant fluid film thickness, the relative velocity between the roller and the discs for each point of the contact area ($\overrightarrow{V_{Rel}}$), can be written as a function of the Slip and Side-slip velocities (V_{Slip} and $V_{Side\text{-}Slip}$ respectively) and the Spin rotation (ω_{Spin}), as shown on Eq.14 (adapted from *Carbone et al.*, 2004).

$$\overrightarrow{V_{Rel}} = \begin{bmatrix} V_{RelX} \\ V_{RelY} \\ 0 \end{bmatrix} = \begin{bmatrix} V_{Slip} \\ V_{Side-Slip} \\ 0 \end{bmatrix} + \omega_{Spin} \cdot \begin{bmatrix} -y \\ x \\ 0 \end{bmatrix} = \begin{bmatrix} V_{Slip} \\ V_{Side-Slip} \\ 0 \end{bmatrix} + \omega_{Spin} \cdot r \cdot \begin{bmatrix} -b_i \cdot \sin\psi \\ a_i \cdot \cos\psi \\ 0 \end{bmatrix} \tag{14}$$

The Spin rotation (ω_{Spin}) can be calculated using the difference between the angular velocities of the bodies in contact, projected in the normal direction of the contact (Raizer, 2010; Carbone *et al.*, 2004). Equation 15 and Eq.16 have information regarding the calculus of Slip and Side-Slip velocities, already considering the angular misalignment due α and β. With those, V_{Slip} and $V_{Side\text{-}Slip}$ are written as a function of the input disk rotation (ω_E), output disk rotation (ω_S), roller rotation (ω_{Rolo}), the contact heights (Y_E for input and Y_S for output), roller radius (r_R) and the angular misalignments Φ_E and Φ_S, calculated with the procedure presented in the previous section.

$$\begin{bmatrix} V_{Slip} \\ V_{Side-Slip} \end{bmatrix}_E = Y_E \cdot \omega_E \cdot \begin{bmatrix} 1 \\ 0 \end{bmatrix} - r_R \cdot \omega_{Rolo} \cdot \begin{bmatrix} \cos\Phi_E \\ \sin\Phi_E \end{bmatrix} \tag{15}$$

$$\begin{bmatrix} V_{Slip} \\ V_{Side-Slip} \end{bmatrix}_S = r_R \cdot \omega_{Rolo} \cdot \begin{bmatrix} 1 \\ 0 \end{bmatrix} - Y_S \cdot \omega_S \cdot \begin{bmatrix} \cos\Phi_S \\ \sin\Phi_S \end{bmatrix} \tag{16}$$

Equation 17 (from Raizer, 2010) relates $\overrightarrow{V_{Rel}}$ and pressure distribution on the contact area with the tangential forces (F_S on the Slip direction and F_{SS} on the Side-slip direction) and the Spin Momentum (normal to the contact area).

$$\begin{bmatrix} F_s \\ F_{ss} \\ M_S \end{bmatrix}_i = a_i b_i \int_0^1 \left(r \cdot \left(\int_0^{2\pi} \frac{\tau_L}{|\overrightarrow{V_{Rel}}|_i} \cdot \left(1 - e^{-\frac{\eta \cdot |\overrightarrow{V_{Rel}}|_i}{\tau_L \cdot H_i}} \right) \cdot \begin{bmatrix} 1 & 0 & 0 \\ 0 & 1 & 0 \\ -b_i \sin\psi & a_i \cos\psi & 0 \end{bmatrix} \cdot \overrightarrow{V_{Rel}}_i d\psi \right) \right) dr \tag{17}$$

The quantity τ_L is the limiting shear stress of the lubricant, normally evaluated for a certain value of the oil temperature, and is given by Eq.18, where τ_{L0} is the limiting shear stress at the atmospheric pressure and p is the punctual pressure exerted on the fluid (Hamrock *et al.*, 2004). Equation 19 enables the evaluation of fluid viscosity (η) over the whole contact region, according to the Roelands model and considering the isothermal contact hypothesis (Carbone *et al.*, 2004). For simplifying purposes, was assumed that the oil film thickness (H_i) is uniform within the contact area, being equal to the film thickness of the contact center (H_c). From Hamrock and Dowson (1981) the H_C formula for hard EHD Lubrication conjunctions is given by Eq.20 (Hamrock *et al.*, 2004).

$$\tau_L = \tau_{L0} + \frac{\partial \tau_L}{\partial p} \cdot p = \tau_{L0} + \zeta \cdot p \tag{18}$$

$$\eta = \eta_0 \cdot \left(\frac{\eta_\infty}{\eta_0} \right)^{1-\left(1+\frac{p}{cp}\right)^{z1}} = \eta_\infty \cdot \left(\frac{\eta_0}{\eta_\infty} \right)^{\left(1+\frac{p}{cp}\right)^{z1}} \tag{19}$$

$$[H_c]_i = \left[2{,}69 \cdot Rx \cdot \left(\frac{V_f \cdot \eta_0}{E_{eq} \cdot Rx} \right)^{0{,}67} \cdot \left(E_{eq} \cdot \frac{z1}{cp} \cdot ln\left(\frac{\eta_0}{\eta_\infty} \right) \right)^{0{,}53} \cdot \left(\frac{Q}{E_{eq} \cdot Rx^2} \right)^{-0{,}067} \cdot (1 - 0{,}61 \cdot e^{-0{,}73k}) \right]_i \tag{20}$$

Where E_{eq} is the equivalent Young Modulus (considering, generically, bodies A and B in contact, with the Young Modules E_A and E_B and Poisson Ratios ϑ_A and ϑ_B, respectively), given by Eq.21, R_x is the equivalent radius of curvature for the contact surfaces at the rolling direction ($R_x{}^{-1} = R_{Ax}{}^{-1} + R_{Bx}{}^{-1}$), V_f is the mean fluid velocity, η_0 is the absolute viscosity at the atmospheric pressure, cp is the Pole pressure constant of Roelands viscosity model, η_∞ is the pole viscosity of Roelands viscosity model, Q is resultant normal loading force at the contact and k is the contact ellipticity ($k = a/b$).

$$E_{eq} = 2 \left(\frac{(1-\vartheta_A{}^2)}{E_A} + \frac{(1-\vartheta_B{}^2)}{E_B} \right)^{-1} \tag{21}$$

2.2. Modeling of pressure mechanism and bearing loss

A good way to promote contact pressure in the T-CVT's automotive application is a mechanical cam combined with a conical spring disc (Machida and Murakami, 2000). The conical disc spring function is to secure the minimum pressure at the contact point even when the input shaft torque is zero or very small. For the normal range of operation of a T-CVT the loading cam is responsible for the system pressurization, giving a linear relation between the input torque (T) and the axial load (F_a), responsible for the normal loading force at the contact (Q) as seen in Eq.22 and in Fig.3. The axial load (F_a) is equally distributed between the rollers at the toroidal cavity (N_{rc} is the number of rollers per cavity) and multiplied by a factor dependant of the contact inclination (δ).

$$Q_i = \frac{F_a}{N_{rc} \cdot sin\ \delta_i} = \frac{2 \cdot \pi \cdot T}{L_c \cdot N_{rc} \cdot sin\ \delta_i} \tag{22}$$

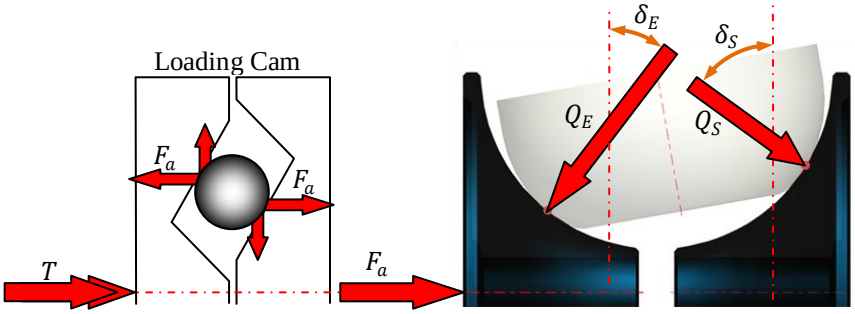

Figure 3. Pressurization of the contacts by a Loading Cam.

At the Roller, the normal contact load Q_E and Q_S are balanced by an axial thrust applied by the roller bearing. In order to estimate torque bearing loss of the power roller bearing the Eq.23 (adapted from Carbone *et al.*, 2004) relates the normal contact loads, projected by the half-cone angle (γ), with T_{BL}. In this equation, Q_E and Q_S are measured in (N) and the torque bearing loss T_{BL} is measured in (Nm).

$$T_{BL} = 4{,}6 \cdot 10^{-5} \cdot [(Q_E + Q_S) \cdot \cos\gamma]^{1{,}03} \tag{23}$$

3. LONGITUDINAL VEHICLE DYNAMICS

The objective of this work is to evaluate the impact new mechanical power source in the performance of a vehicle equipped with T-CVT. For that purpose, a longitudinal vehicle dynamic model were implemented considering the external forces that oppose to the vehicle motion ($\Im$, as a function of the aerodynamic drag, rolling resistance and grading resistance), given by Eq.24 (adapted from Gillespie,1992; Jazar, 2008), and a simplified model for the vehicle powertrain (described in Tab.1, along with the Eq.27 to Eq.44).

$$\Im = \frac{1}{2} \cdot \rho \cdot A_{fCar} \cdot C_D \cdot (V_{Car} + V_{ven})^2 + \left(sin\ \delta_{pi} + \left(fr_0 + fr_1 \cdot {V_{Car}}^2\right) \cdot cos\ \delta_{pi}\right) \cdot M_{Car} \cdot g \tag{24}$$

Where de ρ is the air density (1,2258kg/m³), V_{Car} is the vehicle speed, V_{ven} is the wind velocity, δ_{pi} is the street inclination, g is the gravitational acceleration (9,81m/s²), fr_0 and fr_1 are constants of the rolling resistance model ($fr_0 = 0{,}015$ and $fr_1 = 7 \cdot 10^{-6} s^2 m^{-2}$, from Jazar, 2008). Additional data of the values used in this simulation are displayed at Tab.2. The total brake torque (T_F) and the clutch slip rate (Cr_{emb}) are modeled using Eq.25 and Eq.26 (from Raizer, 2010).

$$T_F = -min\left[\left(T_9 + I_T \frac{\varepsilon_d \cdot \dot{\omega}_9}{{RT_d}^2}\right)\ ;\ 0\right] \tag{25}$$

$$Cr_{emb} = 1 - \frac{\omega_6}{max\left[RT_{Tmin} \cdot RT_{adq} \cdot \omega_{fun}\ ;\ \omega_6\right]} \tag{26}$$

Where: ω_{fun} is the minimum rotational velocity of the ICE's crankshaft and ω_6 is the rotational velocity at the clutch output. The toroidal cavity final TR (RT_T) and efficiency (ε_{tT}) are results from the T-CVT simulation model, and function of the final Slip and Side-slip rate, input torque, the input rotation and the tilt angle (θ). The tilt angle (θ) is determined as a function of the input mechanical power and rotation, using the same methodology described at Raizer (2010).

Table 1. Modeling of the powertrain Sub-Systems (Raizer, 2010).

Sub-System	Speed Ratios Equation	Nº	Torque and Strength Ratios Equation	Nº
Wheels	$r_w \cdot \omega_9 = V_{Car}$	(27)	$\Im = \frac{T_9 - 4 \cdot I_w \cdot \dot{\omega}_9}{r_w} - M_{Car} \cdot \dot{V}_{Car}$	(28)
Brakes	$\omega_8 = \omega_9$	(29)	$T_9 = T_8 - T_F$	(30)
Differential	$RT_d \cdot \omega_7 = \omega_8$	(31)	$T_8 = \frac{T_7 \cdot \varepsilon_d}{RT_d}$	(32)
Driveshaft	$\omega_6 = \omega_7$	(33)	$T_7 = T_6 \cdot \varepsilon_E - I_T \cdot \dot{\omega}_6$	(34)
Clutch	$\omega_5 \cdot (1 - Cr_{emb}) = \omega_6$	(35)	$T_6 = T_5 - C_{embE} \cdot \omega_5$	(36)
Output Reduction	$\omega_5 = RT_S \cdot \omega_4$	(37)	$T_5 = \frac{T_4 \cdot \varepsilon_{tS}}{RT_S}$	(38)
Toroidal Cavities	$\omega_4 = RT_T \cdot \omega_3$	(39)	$T_4 = \frac{T_3 \cdot \varepsilon_{tT}}{RT_T}$	(40)
Input Reduction	$\omega_3 = RT_E \cdot \omega_2$	(41)	$T_3 = \frac{T_2 \cdot \varepsilon_{tE}}{RT_E}$	(42)
Engine	$\omega_2 = \omega_{Eng}$	(43)	$T_2 = T_{Eng} - I_{eng} \cdot \dot{\omega}_{Eng}$	(44)

Table 2. Data for simulation of the vehicle equipped with CVT (Raizer, 2010).

Property	Value	Property	Value
Vehicle Frontal Area, 'A_{fCar}'	$2{,}3m^2$	Differential TR, 'RT_d'	0,2053
Aerodynamic Drag Coefficient, 'C_D'	0,33	Differential Efficiency, 'ε_d'	0,95
Vehicle Total Mass, 'M_{Car}'	$1130kg$	Gearbox-Type	CVT
Tire effective radius, 'r_w'	$0{,}29m$	TR of adequation, 'RT_{adq}'	0,54110
Equivalent Wheel Inertia, 'I_w'	$0{,}4kg.m^2$	Input Reduction TR, 'RT_S'	0,72434
Equivalent Driveshaft Inertia 'I_T'	$0{,}05kg.m^2$	Input Reduction efficiency, 'ε_{tS}'	0,97
Equivalent Engine Inertia, 'I_{eng}'	$0{,}085kg.m^2$	Input Reduction TR, 'RT_E'	0,74697
Driveshaft efficiency, 'ε_E'	0,99	Input Reduction efficiency, 'ε_{tE}'	0,97
Clutch dissipation coefficient, 'C_{embE}'	$0{,}02\ N.m.s/rad$	Cavity Minimum TR, 'RT_{Tmin}'	0,4328
Traction shaft	Front	Cavity Maximum TR, '$RT_{Tmáx}$'	2,3103

Table 3 contains the geometric parameters and material properties for the simulated T-CVT and contains the lubricant properties tested, both adapted from Carbone *et al.* (2004). Any combination of geometric properties, material and lubricant could be used, as long as the final result is capable in transmitting the power, torque and rotation required for the external conditions. The vehicle velocity profile used was determinate considering constant acceleration rate, assuming that the vehicle goes from motionless to *27.8m/s* (*100km/h*) in 25 seconds.

Table 3. Geometrical parameters and material properties of the HT-CVT and Lubricant properties at 99ºC (adapted from Carbone *et al.*, 2004).

Parameter	Value	Parameter	Value
Cavity radius 'R'	40,000mm	Number of rollers per cavity, 'N_{rc}'	2
Roller Profile radius, 'r_a'	32,000mm	Number of cavities, 'N_c'	2
Half-cone angle, 'γ'	60º	Fatigue limiting shear stress, 'τ_u'	276MPa
Torus radius, 'Y_0'	65,000mm	Young's Modulus, 'E'	210GPa
Loading Cam Lead, 'L_c'	17,241mm	Poisson ratios, 'ϑ'	0,3
Absolute viscosity at atmospheric pressure, 'η_0'	$3{,}25 \cdot 10^{-3}$Pa.s	Pole pressure constant of Roelands viscosity model, 'cp'	$1{,}96 \cdot 10^{8}$Pa
Limiting shear stress at atmospheric pressure, 'τ_{L0}'	$0{,}02 \cdot 10^{9}$Pa	Pole viscosity of Roelands viscosity model, 'η_∞'	$6{,}31 \cdot 10^{-5}$Pa
Limiting shear stress constant, 'ζ'	0,085	Viscosity–pressure index, '$z1$'	0,85

3. ELETRIC MOTOR

Variable-speed electric motor drives usually have the characteristics shown in Fig.4. In low-speed operations the motor has a constant torque due to the increase of voltage supply to the motor through the electronic converter while the magnetic flux is kept constant. In the high-speed region (higher than the base speed) the motor voltage is equal to the source voltage and the flux is weakened, keeping delivered power constant and making the torque drop hyperbolically with increasing speed (Ehsani *et al.*, 2005). This characteristic is usually represented by a speed ratio Λ, defined as the

ratio of its maximum speed to its base speed. Each type of motor inherently has its limited maximum speed ratio. For example, a permanent magnet motor has Λ <2 in result from the difficulty of field weakening due to the presence of the permanent magnet. Switched reluctance motors may achieve Λ =6 and induction motors about Λ =4 (Rahman & Ehsani, 1996).

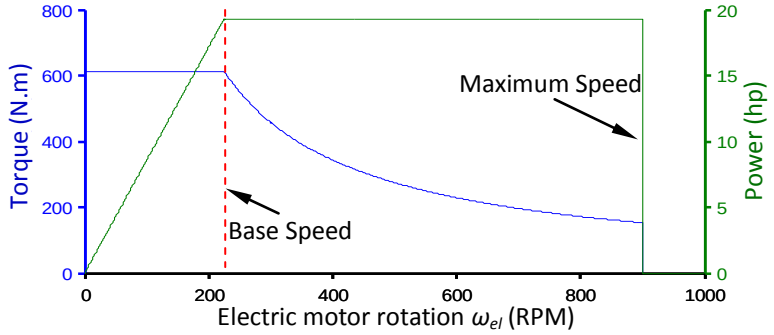

Figure 4. Variable-speed electric motor behavior.

4. RESULTS

In this work, the electrical induction motor (EIM) (Λ =4) used as a hybridization system during simulation has *14,4kW* as maximum power (about *19,3hp*) and maximum rotation of *94,25rad/s* (*900rpm*). The EIM was directly connected (in other words, with the same rotation) to one of the vehicle power train subsystems (described in Tab.1). Three different cases were studied: first, with no additional energy source (conventional ICE vehicle); second, with the EIM directly connected to the traction shaft ($\omega_{el} = \omega_8$); and third, with the EIM directly connected to the driveshaft ($\omega_{el} = \omega_6$). Figure 5 shows the final ICE utilization incidence map for each case. The additional mechanical power brings the ICE to lower Torque and Power operation regions, but affects the T-CVT efficiency due the lack pressurization torque on the cam mechanism described in section 2.2, creating a secondary tendency where mass slip effect occurs. d

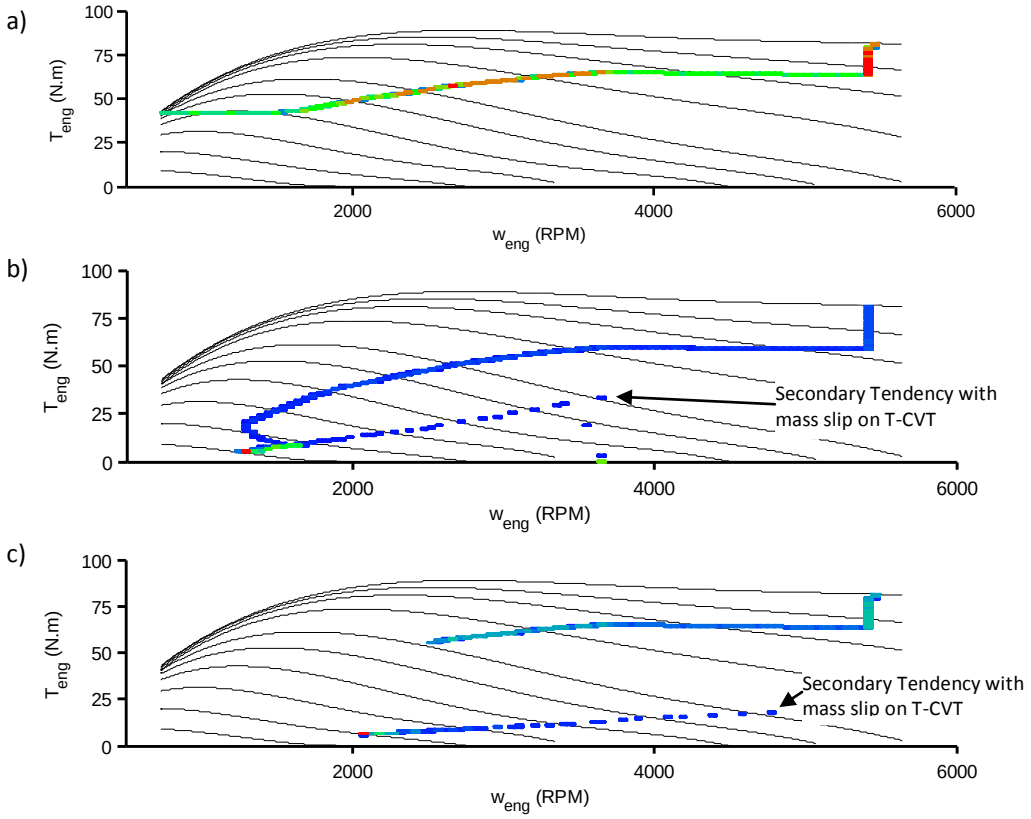

Figure 5. ICE utilization incidence map (Blue: low; Green: medium; Red: high incidence) for regular ICE vehicle (a), HEV with EIM connected to the traction shaft (b) and HEV with EIM connected to the drive shaft (c).

On the regular ICE vehicle behavior, there is a singular tendency of the ICE utilization, where regions of high power (end of the curve, marked as red due high incidence) and high torque with optimum power (middle of the curve, marked as red/orange due high and medium-high incidence) prevail. The global slip coefficient between the output disk and input one (*Cr*, defined by Carbone *et al.*, 2004) remained between *1,4%* and *2,9%*, in other words, the efficiency loss due slip effect was minimal.

At the simulation where the EIM is connected directly to the traction shaft (case 'b' on Fig.5), the electric motor works in *98,9%* of the vehicle speed range (0 to 100km/h). In this case, the electric motor has not enough torque to replace the ICE during is operation, but is enough to bring the high utilization incidence toward lower torque levels. The global slip coefficient *Cr* stood between *81,3%* and *42,0%* until *25km/h*, then it start to fall, reaching *1,5%* to *2,9%* between *38km/h* and *100km/h*.

When an EIM with the same properties is connected to the driveshaft (before the differential TR, case 'c' on Fig.5), the electric motor can work only in *20,3%* of the vehicle speed range, but its torque becomes sufficient to propel the vehicle while being used, acting practically like and EV. In this moment, the *Cr* stood between *96,4%* and *63,4%*. After 20,3km/h the EIM is shut down and the vehicle behavior goes back to a regular ICE vehicle, having a mean *Cr* of *2,1%*.

Figure 6 have information concerning the EIM utilization. It is clear that for case 'c', where the EIM is connected to the drive shaft, that the electric motor has more than enough torque to push the vehicle forward, but only until reach the maximum rotation at *900rpm* (vehicle at *20,3km/h*), when it is forced to shut down. On case 'b', the electric motor is propelling the vehicle alone, until it reaches *318rpm* (vehicle at *35km/h*). The total mechanical energy generated by the EIM during the acceleration process was *292,6kJ* for case 'b', but only *22,4 kJ* for case 'c' (consequence of the early shutdown). By that reason, the relative share of energy that the EIM contributes for the vehicle acceleration for case 'c' is inferior to case 'b', as can be seen on Fig.7.

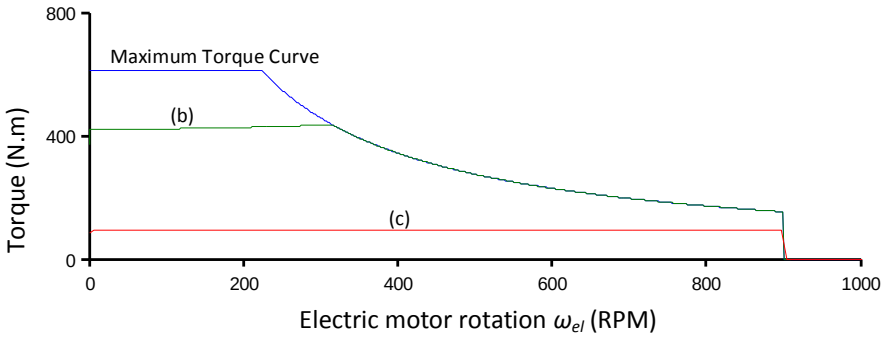

Figure 6. Electric motor utilization during acceleration, for case 'b' and case 'c'.

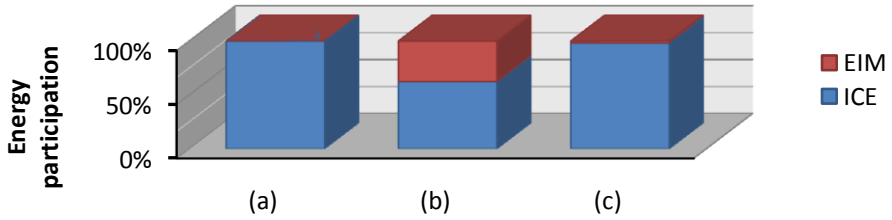

Figure 7. EIM energetic contribution during acceleration, for case 'b' and case 'c'.

5. CONCLUSIONS

The authors conclude that the additional source of mechanical power in a vehicle equipped with a T-CVT can, in fact, reduce the ICE effort in bringing the vehicle from motionless to 100km/h, clearly replacing its function at low speed range. During the electric motor activity, the global efficiency of the toroidal cavity is lower due the lack of pressurization torque at the cam mechanism. The mass slip on the lubricated contacts can cause surface damage. This can be corrected by using and additional pressurization device, like a conical spring disc (Machida and Murakami, 2000), that doesn't rely on the input torque.

With the specific EIM used on simulation, the best result was obtained when it were directly connected to the traction shaft. However, in a practical scenario, a more often use of the electric motor may lead to a high dimensioning of the battery pack, which leads to a heavier vehicle. In this analysis, the weight of the battery pack was considered the same for each simulation, and the results could be different otherwise. A function that relates the total battery pack weight with the electrical energy consumption could be used, creating an iterative process to maximize performance for each possible HEV configuration.

The electric motor torque curve aspect is ideal for low speed operations, where it automatically adapts for a high torque level. But it can clearly aid the ICE performance even at high speed conditions. Of course, that a higher utilization of an electric motor is linked to heavier battery pack. The balance of the necessary battery weight, lower pollutants emission, system final performance, vehicle final cost and even the necessary care in the battery pack disposal (when its life cycle ends) must be considered in order to achieve a cleaner, and environmentally healthier, vehicle.

6. ACKNOWLEDGEMENTS

The authors would like to thank BOSCH, UNICAMP, CAPES, CNPQ and CTI for the support and help.

7. REFERENCES

Attia, N.A., 2005 "Predicting the Life Contact for Half Toroidal Continuously Variable Transmission." Information technology Journal, 222-227, 2005.

Bartilotti, R.R., Genesini, P.R., Raizer, B., Barros de Souza, R., Dedini, F.G., 2009 "Functional Modeling of the powertrain system of a Hybrid Vehicle", SAE paper 2009-36-0258, presented at 2009 SAEBrasil Congress.

Carbone, G.; Mangialardi, L.; Mantriota, G., 2004 "A comparison of the performances of full and half toroidal traction drives", Mechanism and Machine Theory, v.39, 921-942, 2004

Coy, John J.; Loewenthal, S.H.; Zaretsky, E.V., 1976 "Fatigue life analysis for traction drives with appliation to a toroidal type geometry.", Nasa Technical Note, D-8362, pp:1-31.

Ehsani, M., Gao, Y., Gay, S.E., Emadi, A., 2005 "Modern Electric, Hybrid Electric, and Fuel Cell Vehicles", CRC Press, 2005, ISBN 0-8493-3154-4

Forti, A.W., 2003 "Estudo Teórico Experimental de Parâmetros de Projeto de uma Transmissão Continuamente Variável por Tração Tipo Esfera Cone.", PhD. Thesis, FEM-UNICAMP, Campinas-SP, Brazil.

Genta, G., 1997 "Motor Vehicle Dinamics – Modelling and Simulation", World Scientific Publishing Co. Pte Ltd, Singapore, ISBN 9810229119.

Gillespie, T.D., 1992 "Fundamentals of Vehicle Dynamics." Society of Automotive Engineers, Inc. 400 Commonwealth Drive. Warrendale, PA 15096-0001, 1992, ISBN 1-56091-199-9.

Hamrock, B.J., Schmid, S.R., Jacobson, B.O., 2004 "Fundamentals of Fluid Film Lubrication", 2ºEd, Marcel Dekker Inc., New York, 2004, ISBN: 0-8247-5371-2.

Harris, Tedric A.; Kotzalas, Michael N., 2006 "Rolling Bearing Analysis: Essential Concepts of Bearing Technology." CRC Press, Taylor & Francis Group, 5ª ed, 2006, ISBN 978-0-8493-7183-7.

Imanishi, T., Machida, H., 2001 "Development of the POWERTOROS UNIT Half-Toroidal CVT (2) – Comparison between Half-Toroidal and Full-Toroidal CVTs.", NSK Thecnical Journal, n.10, abr. 2001.

Jazar, R.N., 2008 "Vehicle Dynamics: Theory and Application.", Springer, Science+Business Media, LLC, 2008, ISBN 978-0-387-74243-4

Lee, A.P., Newall, J.P., Goto, M., Misada, Y., Ono, Y., 2004, "Experimental Validation of Full Toroidal Fatigue Life." Proceedings of the CVT 2004 Conference - September 23/25, 2004 - San Francisco, USA. 04CVT-21.

Machida, H., Murakami, Y., 2000 "Development of the POWERTOROS UNIT Half Toroidal CVT.", NSK Thecnical Journal, n.9, out. 2000.

Nonato de Paula, F., 2009, "Modelo Dinâmico para o Contato em Mancais de Elementos Rolantes Sujeito à Lubrificação Elastohidrodinâmica.", M.Sc. Dissertation, FEM-UNICAMP, Campinas-SP, Brazil.

Nikas, G.K., 2002 "Fatigue Life and Traction Modeling of Continuously Variable Transmissions.", Journal of Tribology, Transactions of the ASME, v.124, pg.689-698, Oct. 2002.

Raizer, B. and Dedini, F.G., 2009 "Modeling and cinematic analysis of toroidal CVTs: influence of the geometric parameters in performance.", Proceedings of 20th International Congress of Mechanical Engineering (COBEM 2009), Gramado-RS, Brazil. ABCM, 2009. v. COB09. p. 1-8.

Raizer, B. 2010 "Modelagem Modelagem e Análise Cinemática de CVT's Toroidais: Influência dos parâmetros geométricos no desempenho.", M.Sc. Dissertation, FEM-UNICAMP, Campinas-SP, Brazil.

Rahman, K.M., Ehsani, M., 1996 "Performance analysis of electric motor drives for electric and hybrid electric vehicle application", IEEE Power Electronic in Transportation, 49–56, 1996.

Tenberge, P., Möckel, J., 2002 "Toroidal CVT with compact roller suspension." VDI-Berichte, nº1709, p.623-637.

Zhang, Y.; Zhang, X.; Tobbler, W., 2000 "A Systematic Model for the Analysis of Contact, Side Slip and Traction of Toroidal Drives." Journal of Mechanical Design, v.122, p.523-528, December of 2000, S1050-0472(00)01004-7

8. RESPONSIBILITY NOTICE

The following text, properly adapted to the number of authors, must be included in the last section of the paper:
The author(s) is (are) the only responsible for the printed material included in this paper.